




Cite this: *J. Mater. Chem. A*, 2019, 7, 9230

Highly stable lithium–sulfur batteries based on p–n heterojunctions embedded on hollow sheath carbon propelling polysulfides conversion†

Han Zhang,^a Zongbin Zhao,^a *^a Ya-Nan Hou,^a Yongchao Tang,^a Jingjing Liang,^a Xuguang Liu,^b ^b Zhichao Zhang,^c Xuzhen Wang ^{ac} and Jieshan Qiu *^a

Newly-developed lithium–sulfur batteries (LSBs) have been supposed to be extremely promising devices as they deliver a high theoretical energy of 2600 W h kg⁻¹. Utilizing sulfur as the cathode material is advantageous due to its low price, non-toxicity, and abundant resources. The main bottleneck hindering the practical application of LSBs is their poor cycling performance due to the shuttling of soluble lithium polysulfides (LiPSs), poor conductivity, and sluggish redox reaction. Herein, we prepared a new type of p–n heterostructure embedded into carbon hollow nanosheet arrays grown on carbon cloth by subsequent sulfidation and nitridation. The hollow heterostructures can sufficiently restrict the dissolution of LiPSs due to the polar chemisorption and physical confinement, and facilitate polysulfide redox kinetics (Li₂S_x → Li₂S, 2 ≤ x ≤ 8). The abundant active sites and boundary defects constructed by the Co₉S₈–Co₄N heterostructures improve the nucleation/conversion redox kinetics of Li₂S. Also, the hollow structure can increase the sulfur loading and supply enough space for relieving the volume expansion during the whole cycling process. After melting the diffused sulfur of the nanocomposites, the resulting free-standing S/CC@Co₉S₈–Co₄N electrode exhibits a highly stable cycling rate with an ultralow capacity fading rate of 0.027% per cycle at 5.0C over 1000 cycles. Our work provides a potential avenue for constructing heterostructured materials for LSBs with high performance.

Received 25th January 2019
Accepted 8th March 2019

DOI: 10.1039/c9ta00975b

rsc.li/materials-a

1. Introduction

Compared with currently developed alkali metal (Li, Na, K) ion batteries, lithium–sulfur batteries (LSBs) show a higher energy density (2600 W h kg⁻¹) and theoretical specific capacity (1675 mA h g⁻¹).¹ Moreover, the non-toxicity of sulfur, high abundance, and low price make LSBs more appealing.^{2,3} However, the major challenge for realizing the application of LSBs is primarily defeated for the following two reasons, *i.e.*, the polysulfides' dissolution and subsequent shuttling problem.^{4–6} To overcome this issue, various novel host materials having particular physical confinement and chemical adsorption properties have been developed as LSBs' cathodes to restrict the fading rate of the discharge capacity. Along this line, a variety of metal/carbon composite materials such as MnO₂/carbon nanotube,^{7,8} TiO_x/carbon nanosphere,^{9–11} and VO_x/graphene¹²

have been integrated into composite materials with sulfur. The weak force between the polar LiPSs and non-polar carbon limits the capture ability, recycling efficiency, and long-term cycling stability.^{1,13,14} All these metal/carbon-based host materials greatly enhance the conductivity of electrodes and limit the shuttle effect of LiPSs' diffusion effectively. Furthermore, the rational design of host nanostructures has been widely investigated for polysulfide trapping.^{15–17}

The other reason of capacity fading is the slow kinetics of cell reaction.¹⁸ To solve this problem, the most effective way is to improve the electrode conductivity and provide active sites to improve the nucleation/conversion redox kinetics.⁸ Some sulfides (WS₂,¹⁹ CoS₂,²⁰), oxides (La₂O₃,²¹ Fe₂O₃,²²), nitrides (WN,²³ TiN²⁴) and metal-free polar materials (phosphorene,²⁵ p-C₃N₄,²⁶) are found to be able to form strong chemical bonds with LiPSs as well as catalytically promote the conversion of the long-chain LiPSs to Li₂S₂/Li₂S, indicating a rational way for the construction of LSBs' electrode materials.

Recently, constructing functional heterostructures has emerged and has immense potential in improving the physical/chemical properties of materials for catalysis^{27–29} and energy conversion and storage.^{30–33} The Yang group proposed a TiO₂–TiN heterostructure project to construct a highly active interface for realizing the trapping and promoting the conversion of LiPSs.^{34,35} Furthermore, benefiting from the internal electric

^aState Key Lab of Fine Chemicals, Liaoning Key Lab for Energy Materials and Chemical Engineering, PSU-DUT Joint Center for Energy Research, School of Chemical Engineering, Dalian University of Technology, Dalian 116024, China. E-mail: zbzhaodlut.edu.cn; jqiu@dlut.edu.cn

^bKey Lab of Interface Science and Engineering in Advanced Materials, Ministry of Education, Taiyuan University of Technology, Taiyuan 030024, China

^cSchool of Chemistry, Dalian University of Technology, Dalian 116024, China

† Electronic supplementary information (ESI) available. See DOI: 10.1039/c9ta00975b

field at the heterointerfaces, p–n heterostructures can promote charge transport and improve the reaction kinetics.³² Tong *et al.* successfully constructed the n-type Ni₃N and p-type Ni₃S₂ that contributed to additional lithium storage, leading to a synergistic effect *via* the faster extraction and insertion of lithium ion due to the outstanding conductivity of Ni₃N and enhanced diffusion controlled capacity of Ni₃S₂.³⁶ However, the feasible construction of p–n heterostructures with multiple functions such as high catalytic activity, efficient sulfur capture capability, and high conductivity remains a great challenge.

Herein, the *in situ* creation of cobalt sulfide–nitride heterostructures embedded hollow nanosheet arrays on carbon cloth from ZIFs for high performance LSBs is reported for the first time. The unique Co₉S₈–Co₄N heterostructures constructed by the sulfidation–nitridation of the ZIF precursor possess the following advantages: (i) the unique nanosheet with inner cavities not only shortens the transport paths for the ions/electrons but also structurally confines the soluble LiPSs' dissolution; (ii) the highly polar Co₉S₈–Co₄N heterostructures can strongly absorb LiPSs and restrain their outward diffusion into the electrolyte; (iii) the new type of p–n heterostructures provide abundant active sites and boundary defects while improving the nucleation/conversion redox kinetics and reducing the overpotential of Li₂S nucleation. As a result, the carbon cloth-based (CC) free-standing electrode has a high capacity and is appropriate for the construction of flexible LSBs. With a high areal mass loading of 1.4–2.0 mg cm^{−2}, the free-standing S/CC@Co₉S₈–Co₄N cathode exhibits a discharge capacity of 1137 mA h g^{−1} at 0.5C (1C = 1675 mA h g^{−1}) over 100 cycles, a high rate capacity of 648 mA h g^{−1} at 5.0C, and retains an ultralow capacity fade rate of 0.027% per cycle over 1000 cycles at 5.0C. Such heterostructures may provide a new pathway in the fields of electrochemical energy storage and catalysis.

2. Experimental

2.1 Synthesis of CC@ZIF-67 nanosheet array precursor

Carbon cloths (CC, 2 × 2 cm) were firstly exposed to oxygen plasma generated by a pulsed power supply (200 W) for 6 min and washed with ethanol and acetone several times, then immersed in 100 mL deionized water containing 0.72 g Co(NO₃)₂·6H₂O and 1.64 g 2-methylimidazole (2-MeIm) without disturbance. After 4 h of reaction at room temperature (RT), the product was washed with water, leading to the formation of CC@ZIF-67.

2.2 Synthesis of CC@Co₉S₈ hollow nanosheet arrays

Typically, 180 mg of thioacetamide (TAA) was dispersed into 60 mL absolute ethanol and stirred for 10 min. Then, a piece of CC@ZIF-67 (2 × 2 cm) was added into the above solution and transferred into a 100 mL Teflon-lined autoclave and maintained at 120 °C for a series of sulfidation times ranging from 0.5 to 4 h. The resulting product was washed with water and ethanol, and dried at 60 °C for 12 h. The product was heated to 600 °C at a heating rate of 2 °C min^{−1} and the temperature was

maintained for 2 h in flowing Ar atmosphere, leading to the formation of CC@Co₉S₈ hollow nanosheet arrays.

2.3 Synthesis of the CC@Co₉S₈–Co₄N heterostructures hollow nanosheet arrays

The as-prepared CC@Co₉S₈ was heated to 600 °C at 2 °C min^{−1} in a tube furnace and maintained for different time durations (1, 2, 3, and 4 h) at the final temperature under the NH₃ flow rate of 50 sccm. The as-prepared Co₉S₈–Co₄N heterostructures on carbon cloth were denoted as CC@Co₉S₈–Co₄N. Without special explanation, the nitridation time is 2 h.

2.4 Synthesis of CC@Co₄N-porous carbon nanosheet arrays

Typically, a piece of CC@ZIF-67 was mounted into a tube furnace and heated to 600 °C at 2 °C min^{−1} for 2 h in N₂ atmosphere. After cooling to the room temperature, the temperature was raised to 330 °C at 10 °C min^{−1} and maintained at this temperature for 2 h in air, then increased to 600 °C at 2 °C min^{−1}, and kept at this final temperature for 3 h under a flowing NH₃ (50 sccm). The as-prepared Co₄N embedded porous carbon nanosheet arrays on carbon cloth were denoted as CC@Co₄N.

2.5 Synthesis of CC@porous carbon nanosheet arrays

The CC@ZIF-67 was heated to 600 °C at 2 °C min^{−1} for 2 h in N₂ atmosphere. The obtained product was kept in a sulfuric acid solution (1 M) solution for 24 h to remove the Co metal nanoparticles and was noted as CC@PCNA.

2.6 Synthesis of the ZIF-67, Co₉S₈, Co₄N, and Co₉S₈–Co₄N

For the synthesis of ZIF-67, 0.72 g Co(NO₃)₂·6H₂O and 1.64 g 2-MeIm were added into deionized water (100 mL). After thorough mixing, the solution was incubated at RT for 4 h. The resulting purple precipitate was centrifugation, washed with ethanol several times, and dried at 70 °C overnight. The Co₉S₈, Co₄N, and Co₉S₈–Co₄N were prepared from ZIF-67 using the same procedure as for CC@Co₉S₈, CC@Co₄N, and CC@Co₉S₈–Co₄N, except the presence of the carbon cloth.

2.7 Synthesis of the sulfur composites

Sublimed sulfur (0.15 g) was added into 10 mL CS₂ and CC@Co₉S₈–Co₄N was fully soaked into the CS₂ solution for 15 min, followed by drying at 60 °C overnight. Then, the CC@Co₉S₈–Co₄N composite was heated under Ar atmosphere at 155 °C for 12 h in stainless steel vessels, with a sulfur mass loading of 1.4–6.1 mg cm^{−2} (Fig. S18†). Thermogravimetric analysis (TGA) reveals the sulfur content in the S/CC@Co₉S₈–Co₄N electrode to be 14.52%. The S/CC@Co₉S₈, S/CC@PCNA, and S/CC composites were prepared by the same procedure.

2.8 Bottle-cell experimental test

Bottle cells were fabricated with S/CC@Co₉S₈–Co₄N, S/CC@Co₉S₈, and S/CC (2 × 2 cm) composites as the cathode materials, Li foil as the anode, and 1.0 M LiTFSI in DOL/DME

(1 : 1 by volume) with 2 wt% LiNO₃ as the electrolyte. The cell tests were conducted at the current rate of 0.5C.

2.9 Assembly of the Li₂S₆ symmetric cells

The symmetric cells were prepared with Li₂S₆ solution as the sulfur source. The Li₂S₆ catholyte was prepared by adding Li₂S and S into the electrolyte at a molar ratio of 1 : 5. The Co₉S₈ and Co₉S₈-Co₄N (0.5 mg cm⁻²) were loaded onto the carbon fiber paper (CP). 40 μL 0.5 M Li₂S₆ electrolyte was added into each coin cell. The CV and EIS tests were carried out by a CHI760E electrochemical workstation. CV was performed at a scan rate of 50 mV s⁻¹ in the voltage range of -0.8–0.8 V.

2.10 Measurement of the Li₂S nucleation

The Li₂S₈ solution was prepared by adding Li₂S and S into the electrolyte (tetraglyme solvent with additional 1.0 mol L⁻¹ LiTFSI) with a molar ratio of 1 : 7. The Co₉S₈ and Co₉S₈-Co₄N (2 mg cm⁻²) were loaded onto the CP as cathode while the lithium foil was the anode. 20 μL Li₂S₈ (0.2 M) catholyte was added into the cathode side, while 20 μL blank electrolyte without Li₂S₈ was added in the anode side. The cell was first galvanostatically discharged at the current of 0.112 mA until the voltage reached 2.06 V, then the voltage was held at 2.05 V until the current decreased to 10⁻⁵ A.

2.11 Characterization

The morphology, composition, and structure of the products were characterized by FE-SEM (SUPARR 55), TEM (JEM-2000EX), HR-TEM (G2 20), XPS (Thermo ESCALAB 250, Al Kα X-ray source), XRD (Rigaku D/MAX-2400, Cu Kα X-ray source), Raman (DXR), TGA (DTG-60AH), ICP (PerkinElmer Nex ION 300D), and elemental analysis (Vario EL III).

2.12 Electrochemical measurements

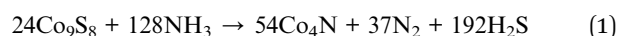
The sample composites were fabricated into 2025 coin-type cells. The coin-type cells were assembled in a glove box under argon atmosphere (water and oxygen concentration less than 0.1 ppm). The Li-S batteries consist of a prepared electrode, polypropylene separator, and lithium foil as the counter electrode. The electrolyte used in this experiment was a 1.0 M solution of LiTFSI in DOL/DME (1 : 1 by volume; TFSI = bis(trifluoromethylsulfonyl)imide; DOL = 1,3-dioxolane, DME = dimethylether) with 2.0 wt% LiNO₃ additive. The amount of electrolyte in a cell is 45 μL. The galvanostatic charge/discharge tests were carried out on a Land CT2001A battery test system between 1.7–2.8 V. The cyclic voltammograms and electrochemical impedance spectroscopy were conducted using a multichannel electrochemical workstation (VMP-300 and CHI760E) between 1.7 and 2.8 V at a scan rate of 0.1 mV s⁻¹.

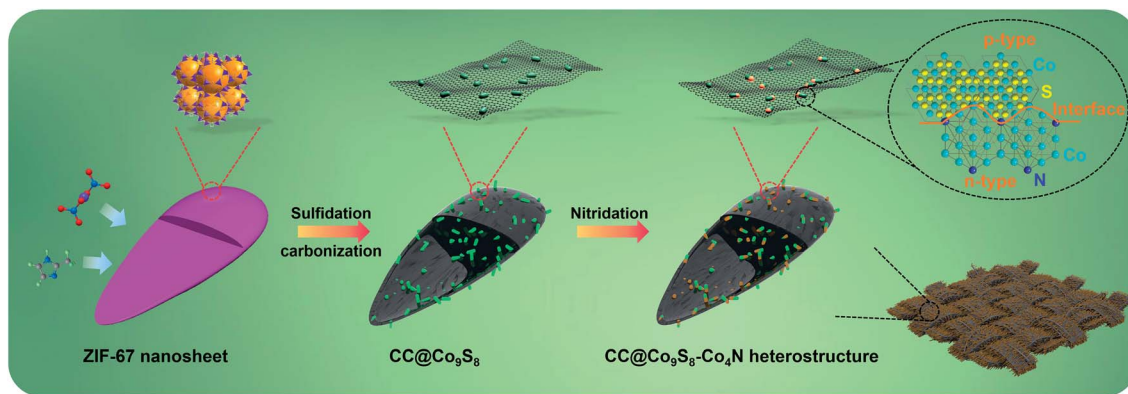
3. Results and discussion

Scheme 1 illustrates the synthetic process of CC@Co₉S₈-Co₄N heterostructures hollow nanosheet arrays involving three steps. Firstly, an oxygen plasma treatment improves the hydrophilicity

of the carbon cloth (Fig. 1a),³⁷ and enriches the surface of the carbon cloth with oxygen-containing groups (–O–C, C=O, –O–C=O). These functional groups can provide numerous nucleation sites for ZIF crystal seeds, leading to the formation of a strong bonding force between the ZIFs and the carbon cloth surface. The untreated-CC is found to be very hydrophobic with a contact angle of about 125°. In contrast, the plasma activated CC becomes very hydrophilic with the contact angle reduced to 60° (Fig. S1†). Then, the 2D ZIF nanosheets vertically grown on CC are achieved by immersing CC into a solution of Co(NO₃)₂·6H₂O and 2-methylimidazole (2-MeIm). The digital image of CC@ZIF-67 is shown in Fig. S2.† The field emission scanning electron microscopic (FE-SEM) images in Fig. 1b and S3† indicate the uniform coverage of the vertically oriented ZIF nanosheet arrays grown on the carbon cloth surface. From the high-magnification FE-SEM images in Fig. 1b and d, one can see the compact solid nature of these ZIF-67 nanosheets with smooth surfaces, whose average thickness is 170 nm and width is 1.7 μm. The X-ray diffraction (XRD) pattern of the CC@ZIF-67 in Fig. 3a matches well with that of the simulated ZIF-67 crystals. In addition, free 2D ZIF-67 nanosheets (Fig. S4†) were also prepared in the absence of the carbon cloth, which are remarkably larger than those on the CC. In the second step, after sulfidation and carbonization, the product inherits the sword-like nanosheet morphology and homogeneous size from the CC@ZIF-67 precursor (Fig. 1c and S5a†). However, through an exchange reaction between the S²⁻ and Co ions with a mechanism similar to the Kirkendall effect (Fig. S6†),^{38–40} the structure evolves from solid to hollow sheath, which is revealed by FE-SEM and transmission electron microscopic (TEM) characterizations (Fig. 1e–h). The average thickness of the sheath shrinks from that of the original ZIF-67 nanosheets (170 nm) to about 149 nm. The hollow structure could enhance the utilization of sulfur, accommodate the volume expansion, and provide a larger void space for high sulfur loading.^{41,42} It is worth mentioning that the short-duration (1, 2 h) TAA etching process results in both the compact and hollow structures, while excess etching time (2, 4 h) leads to severe etching and incomplete structures, even the destruction of the 2D ZIF nanosheets (Fig. S6†). The XRD pattern of CC@Co₉S₈ shows that the diffraction peaks correspond to those of Co₉S₈ (JCPDS No. 86-2273, Fig. 3a). High-resolution TEM (HR-TEM) image of the hollow nanostructure is shown in Fig. S5b; † the observed lattice fringes with the spacing of 0.299 nm is indexed to the (311) plane of Co₉S₈.⁴⁰ In contrast, the direct calcination of CC@ZIF-67 at 600 °C under a N₂ atmosphere without sulfidation, followed by acid etching results in the formation of the porous carbon nanosheet arrays on the carbon cloth (noted as CC@PCNA, Fig. 1f–i), while the Co₄N embedded porous carbon nanosheet arrays (CC@Co₄N) were prepared using the modified method reported previously (Fig. S7†).⁴³

In the third step, we executed the nitridation of CC@Co₉S₈ with NH₃ (50 sccm), where the compound phase transformation from Co₉S₈ to Co₄N under NH₃ atmosphere occurs *via* the following equation:





Scheme 1 Schematic illustrations showing the fabrication of $\text{CC@Co}_9\text{S}_8\text{-Co}_4\text{N}$ heterostructures hollow nanosheet arrays.

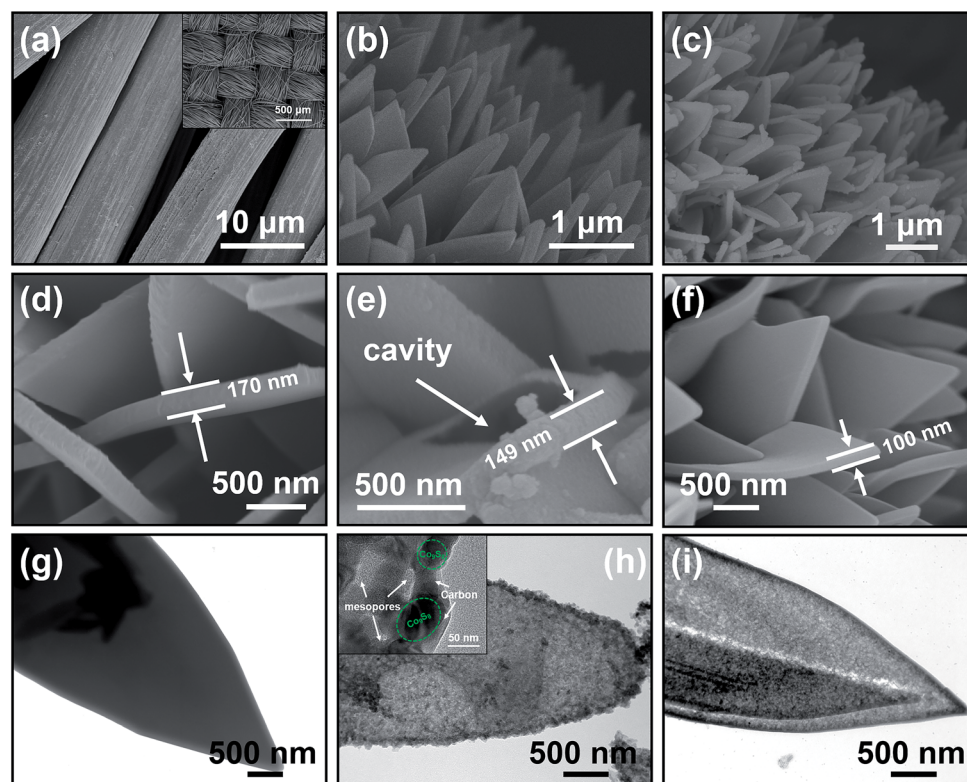


Fig. 1 FE-SEM images of (a) O_2 -plasma treated carbon cloth, (b and d) CC@ZIF-67 , (c and e) $\text{CC@Co}_9\text{S}_8$, and (f) CC@PCNA . TEM images of (g) CC@ZIF-67 , (h) $\text{CC@Co}_9\text{S}_8$, and (i) CC@PCNA .

After the nitridation, a part of Co_9S_8 ($Fm\bar{3}m$ (225)) was converted to Co_4N ($Pm\bar{3}m$ (221)), in which the N atom takes the position at the body centers (inset of Fig. 3c and S8†). As depicted in Fig. S9,† in the XRD profile of the obtained $\text{Co}_9\text{S}_8\text{-Co}_4\text{N}$ heterostructures, the Co_4N characteristic peak (JCPDS No. 41-0943) is shifted to smaller diffraction angles compared to cobalt element (JCPDS No. 15-0806), implying the lattice expansion attributed to the incorporation of the N atoms into the Co lattice.^{44,45} The experimental parameters were carefully explored *via* control experiments. With the increasing nitridation time, Co_2C was observed, resulting from the reaction of the

Co species with CO *in situ* released from the decomposition of the carbon nanosheets (Fig. S10†).⁴⁶ As shown in Fig. 2a–c, on the surface of the carbon cloth, a large number of vertically oriented sheet structures were seen, which had a diameter of *ca.* 65 nm and maintained the overall sheet-like structure after the nitridation process. The hollow morphology can be well preserved and the porous structure can be clearly observed (Fig. 2d). The HR-TEM image consists of the different lattice spaces and the phase boundaries between the Co_9S_8 and Co_4N consisted of the same plane, suggesting the uniform formation of the Co_9S_8 and Co_4N interfaces within the nanosheets

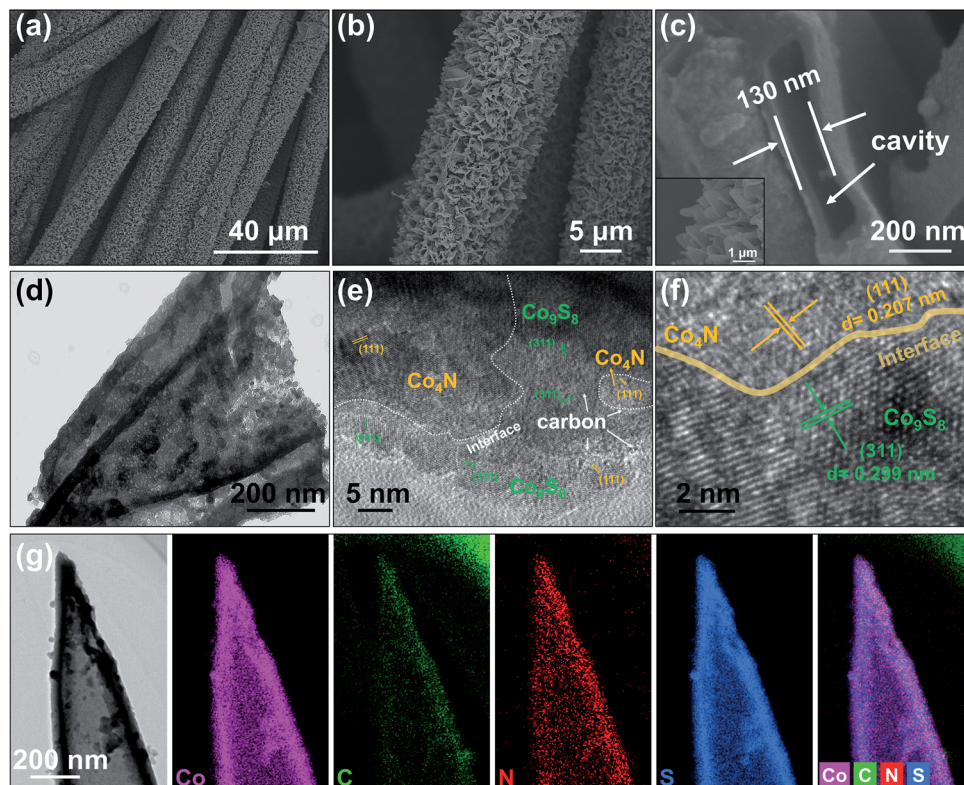


Fig. 2 (a–c) FE-SEM images of CC@Co₉S₈–Co₄N. (d) TEM and (e and f) HR-TEM images of the CC@Co₉S₈–Co₄N hollow nanosheet. (g) TEM image of CC@Co₉S₈–Co₄N and the corresponding elemental maps of Co, C, N, and S.

(Fig. 2e). As shown in Fig. 2f, the lattice spacings of 0.299 and 0.207 nm were indexed to the (311) and (111) planes of Co₉S₈ and Co₄N, respectively,^{47,48} and the (311) and (111) peaks are in good agreement with the XRD patterns of CC@Co₉S₈–Co₄N (Fig. 3a). Moreover, Fig. 2f shows a distinct interface between the (311) plane of Co₉S₈ and the (111) plane of Co₄N, which benefits the ion transportation and LiPSs conversion.^{30,35} Elemental mappings of Co, C, N, and S correspond well to the profile of the nanosheet in Fig. 2g, indicating the uniform distribution of these elements in the materials. Based on the inductively coupled plasma (ICP) and elemental analysis measurements, the average weight content of Co, N, and S in the CC@Co₉S₈–Co₄N was 4.50%, 2.53%, and 12.96% (Table S1†). After loading sulfur, for the S/CC@Co₉S₈–Co₄N composite, no obvious peak of the element S can be found (Fig. S11a†) and the TEM image showed that the darker contrast of the inside region of the S/CC@Co₉S₈–Co₄N composite indicates the diffusion of sulfur into the inner space (Fig. S11b†), implying that sulfur is distributed well in the CC@Co₉S₈–Co₄N composite. For comparison, after successively annealing the CC@ZIF-67 under N₂ and NH₃, the sword-like morphology can be well preserved but a porous structure can be clearly observed and the surface of nanosheets become rough and porous after treatment under flowing NH₃ at 600 °C (Fig. S7a and b†). As shown in Fig. S7c,† after the nitridation process, the cubic Co₄N (PDF#41-0943) with (111), (200), and (220) planes appears, which suggests the transformation of ZIF-67 to Co₄N.

The Raman spectra of CC@Co₉S₈–Co₄N are shown in Fig. 3b, in which the vibrational modes of Co, such as E_g (471 cm⁻¹), F_{2g} (515 and 605 cm⁻¹), and A_{1g} (672 cm⁻¹) are observed. Compared with the CC@Co₉S₈, the E_g and A_{1g} characteristic peaks of CC@Co₉S₈–Co₄N were shifted from 471 and 672 cm⁻¹ to 482 and 691 cm⁻¹, respectively.⁴⁹ These major shifts are mainly attributed to the fact that the features of the newly transformed Co₄N with the shrunken interlayer spacing give rise to an increased interlayer van der Waals force, which would result in a weaker out-of-plane vibration.⁵⁰

The Mott–Schottky plot is usually used to identify the type of semiconductor. Fig. 3c shows that the Mott–Schottky slope of the Co₄N is > 0 and that of Co₉S₈ is < 0, indicating that Co₉S₈ is a p-type semiconductor and Co₄N is a n-type semiconductor.^{51,52} As previously reported,³⁶ not only do the boundaries of the p–n heterojunction provide active sites and defects but also the electrons in the n-type semiconductor tend to transfer to the p-type semiconductor, leading to a preferable separation of the lithium ions and the electrons and thus, a great electrochemical performance. X-ray photoelectron spectroscopy (XPS) was executed to survey the chemical states of the CC@Co₉S₈ and CC@Co₉S₈–Co₄N composites. The XPS survey spectra imply that the as-prepared materials consist of C, Co, N, S, and O (Fig. S12†). The presence of oxygen could be attributed to the unavoidable surface oxidation of the samples in air. The high-resolution N 1s spectrum is shown in Fig. 3d; CC@Co₉S₈ has crudely doped N atoms at various sites with

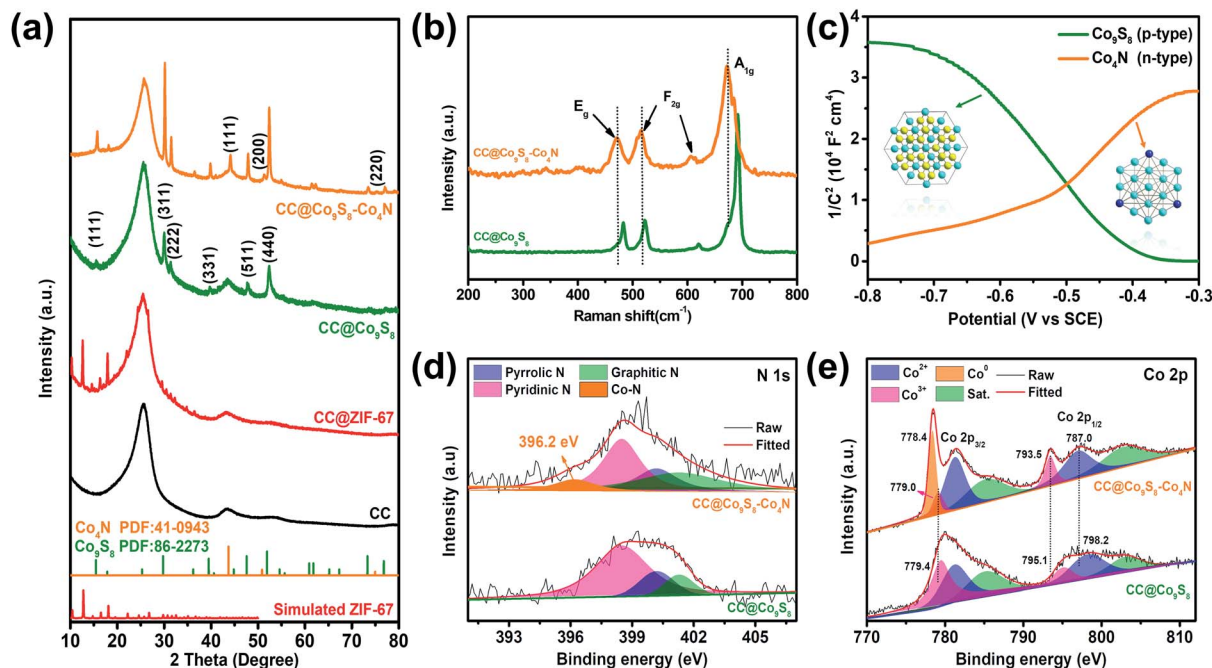


Fig. 3 (a) XRD patterns of CC, CC@ZIF-67, CC@Co₉S₈, and CC@Co₉S₈-Co₄N. (b) Raman spectra of CC@Co₉S₈ and CC@Co₉S₈-Co₄N. (c) Mott-Schottky plots of Co₉S₈ and Co₄N tested at each potential with 1000 Hz frequency in 0.5 M Na₂SO₄ electrolyte (inset are the unit cells of Co₉S₈ and Co₄N structures). (d and e) High resolution N 1s and Co 2p XPS spectra of CC@Co₉S₈-Co₄N and CC@Co₉S₈.

pyridinic N (398.5 eV), pyrrolic N (400.2 eV), and graphitic N (401.3 eV), derived from the carbonization of C=N=C and C-N-C groups of 2-MeIm.⁵³ These inherent N-doped atoms in the carbon nanosheets might be good for strengthening the adsorption capacity of the LiPSs.^{54,55} After the nitridation process, all the peaks in the N 1s region were entirely retained and a new peak emerged at 396.2 eV ascribed to the Co-N bonds.⁵⁶ In the Co 2p spectra, the binding energy located at 779.0 eV and 793.5 eV corresponds to the spin-orbit characteristics of Co³⁺, while those at 781.3 eV in Co 2p_{3/2} and 797.0 eV in Co 2p_{1/2} are attributed to Co²⁺ (Fig. 3e).⁵⁷ It should be noticed that a sharp peak of Co⁰ (778.4 eV) was clearly observed in CC@Co₉S₈-Co₄N compared with CC@Co₉S₈.⁴⁴ More interestingly, the lower binding energies (~0.4 and 1.2 eV) of the Co 2p_{3/2} and Co 2p_{1/2} peaks in CC@Co₉S₈-Co₄N are also observed compared with those of CC@Co₉S₈, proposing a strong interaction between the Co₉S₈ and the Co₄N,⁵⁸ which is in agreement with the previous Raman spectra results.

The coin cells were fabricated with the as-prepared composites (loaded with S) as the cathode material and lithium foil as the anode. The cyclic voltammetric (CV) measurements were executed at different scan rates from 0.1 to 1.0 mV s⁻¹ to explore the kinetics of Li⁺ insertion/extraction and Li⁺ diffusion rate in the battery, in which the S/CC@Co₉S₈ and S/CC@Co₉S₈-Co₄N composites were assessed within a voltage window of 1.7–2.8 V *versus* Li/Li⁺ (Fig. 4a and b). All the anodic and cathodic peak currents maintain a linear relationship with the square root of scan rates (Fig. 4c). The Li⁺ diffusion capability can be obtained using the classical Randles-Sevcik equation:⁵⁹

$$I_p = 2.69 \times 10^5 n^{1.5} a D_{Li^+}^{0.5} C v^{0.5} C_{Li} \quad (2)$$

where I_p is the peak current, n is the number of electrons in the reaction, a is the electrode area, D_{Li^+} is the Li⁺ diffusion coefficient, v is the scan rate, and C_{Li^+} is the Li⁺ concentration in the electrolyte. The relationship between the slopes of the curves and the corresponding Li⁺ diffusion is positive correlation. From the linear relationship of $v^{1/2}$ and I_p , the obtained Li⁺ diffusion coefficient of the materials is shown in Fig. 4d. For the S/CC@Co₉S₈-Co₄N cathode, $D_{Li^+}^{A1} = 8.6 \times 10^{-13}$,

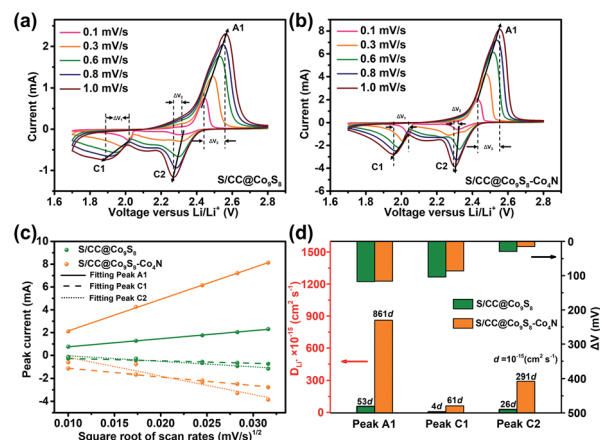


Fig. 4 CV curves of (a) S/CC@Co₉S₈ and (b) S/CC@Co₉S₈-Co₄N cathodes obtained in the range of 0.1–1.0 mV s⁻¹. (c) Peak currents *versus* square root of scan rates of S/CC@Co₉S₈ and S/CC@Co₉S₈-Co₄N. (d) Polarized voltage and Li⁺ diffusion coefficient comparison of the S/CC@Co₉S₈ and S/CC@Co₉S₈-Co₄N composites.

$D_{\text{Li}^+}^{\text{C1}} = 6.1 \times 10^{-14}$, and $D_{\text{Li}^+}^{\text{C2}} = 2.9 \times 10^{-13} \text{ cm}^2 \text{ s}^{-1}$ are obtained, which are over 10 times higher than that of the S/CC@Co₉S₈ cathode. The significant enhancement shown by S/CC@Co₉S₈-Co₄N in Li⁺ diffusion kinetics may be ascribed to several reasons: (i) heterostructures restrict the growth of crystalline domains and could shorten the Li⁺ diffusion pathway;^{60–62} (ii) ZIF derived hollow carbon skeleton makes the Co₉S₈/Co₉S₈-Co₄N nanoparticles' distribution more uniform and effectively restrains the nanoparticles from aggregation;⁶³ (iii) more importantly, in the p-n heterojunction, the preferable separation of the lithium ions and electrons is enhanced by the boundary effect, which provides more active sites.³⁶

Besides, it can be shown that the distinguishable shift of the intensive polarized voltage (ΔV) appears with the increase in the scan rate during the fast charge-discharge process. It has been known that the polarization of the electrode results in the reduction of specific capacitance (Fig. 4d);⁶⁴ in the case of S/CC@Co₉S₈-Co₄N, it possesses a smaller ΔV compared with S/CC@Co₉S₈, therefore, we can easily understand the reason for the best stability and highest capacity of S/CC@Co₉S₈-Co₄N.^{65,66}

Fig. 5a shows the CV tests of S/CC@Co₉S₈ and S/CC@Co₉S₈-Co₄N at 0.1 mV s⁻¹ in the range of 1.7–2.8 V. The CV curves of the samples exhibit two cathodic peaks and one anodic peak corresponding to the redox reaction of LSBs. Specifically, the cathodic peaks C2 (2.32 V) and C1 (2.04 V) correspond to the reduction of S₈ to Li₂S_n ($4 \leq n \leq 8$) and the further conversion of

Li₂S_n ($4 \leq n \leq 8$) to Li₂S₂/Li₂S. On the other hand, the anodic peak A1 (2.42 V) was associated with the oxidation of Li₂S to S₈.⁶⁷ Obviously, the peaks of S/CC@Co₉S₈-Co₄N are much narrower and stronger compared with those of S/CC@Co₉S₈, indicating significantly enhanced reactions at these potentials.^{22,68} Meanwhile, compared with S/CC@Co₉S₈, the anodic peak of the S/CC@Co₉S₈-Co₄N heterostructure shifts to a lower potential and the cathodic peaks shift are positively deviation, suggesting the decreased activation energy. It can be concluded that the heterostructures promote the conversion of the long-chain LiPSS to Li₂S₂/Li₂S, clearly demonstrating their catalytic activity during this process.²² As a result, the possibility of shuttling of the LiPSSs is efficiently restrained. Moreover, the distances between the A1 and C1 peaks are 0.38 V and 0.43 V for S/CC@Co₉S₈-Co₄N and S/CC@Co₉S₈, respectively, implying improved polarization, which is in harmony with the follow-up experimental results and previous heterostructure studies.^{31,34}

The cycling test of the five electrodes was evaluated at 0.5C within the voltage window of 1.7–2.8 V (Fig. 5b). Benefitting from the high conductivity, the special hollow structure and p-n heterojunction of CC@Co₉S₈-Co₄N, the free-standing cathodes show outstanding capacity and cycling performances. The initial discharge capacity is 933 mA h g⁻¹, and from the second cycle onwards, the capacities of the S/CC@Co₉S₈-Co₄N electrodes slowly increases from 930 to 1137 mA h g⁻¹ within 100 cycles, while the discharge of S/CC@Co₉S₈, S/CC, S/CC@PCNA,

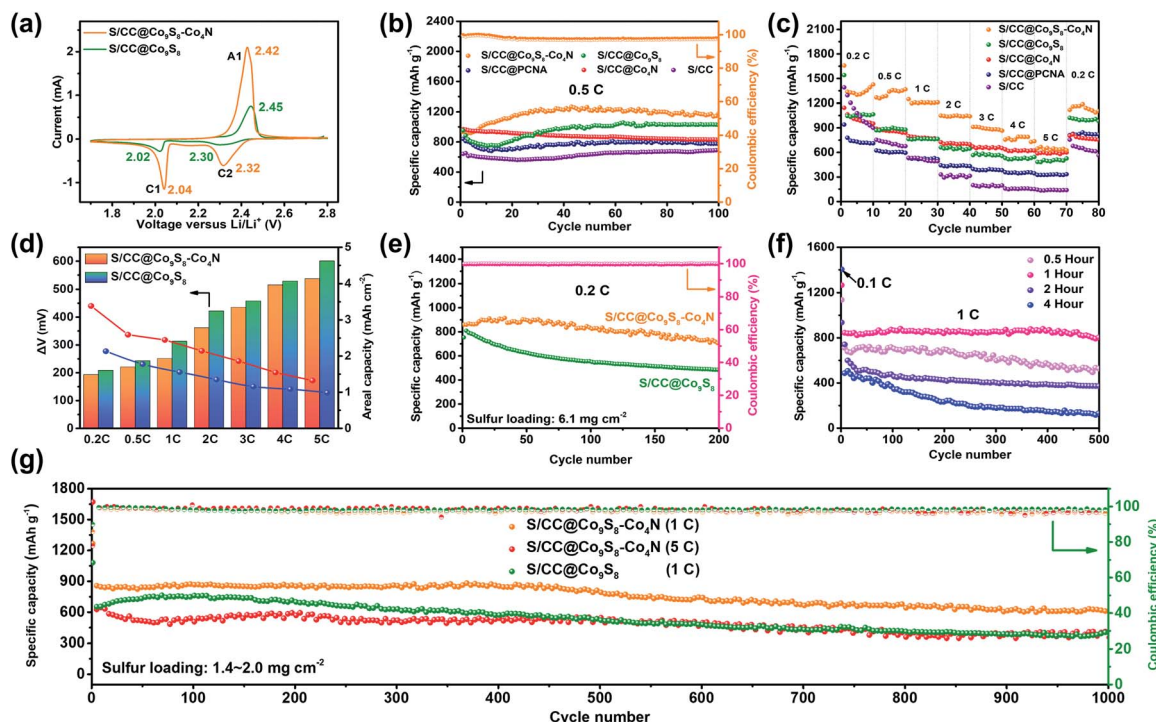


Fig. 5 (a) Cycling voltammogram curves, (b) cycling performance at 0.5C, and (c) rate capabilities of the S/CC, S/CC@Co₄N, S/CC@PCNA, S/CC@Co₉S₈, and S/CC@Co₉S₈-Co₄N electrodes. (d) Comparison of the polarization voltage between the discharge and charge plateaus and areal capacity of S/CC@Co₉S₈ and S/CC@Co₉S₈-Co₄N at different current densities. (e) Cycling performance of the S/CC@Co₉S₈-Co₄N and S/CC@Co₉S₈ at 0.2C over 200 cycles with high sulfur loading of 6.1 mg cm⁻². (f) Long-term cycling performance of S/CC@Co₉S₈-Co₄N with different sulfidation time (0.5, 1, 2, and 4 h) at 1C. (g) Long-term cyclability of S/CC@Co₉S₈ at 1.0C and S/CC@Co₉S₈-Co₄N at current densities of 1.0 and 5.0C.

and S/CC@Co₄N drop to 1030, 690, 770, and 831 mA h g⁻¹ after 100 cycles, respectively. On the other hand, the S/CC@Co₉S₈-Co₄N electrode delivers a much higher initial coulombic efficiency (99.58%) in comparison with the S/CC@Co₉S₈ composite (93.20%), which approaches nearly 100% after several cycles. This reveals that the heterostructures greatly alleviate the polysulfide shuttle effect and keep the polysulfide within the cathode region, leading to good cycling stability. Moreover, compared with S/CC and S/CC@Co₉S₈, the traces of dissolved LiPSs on the separator from the S/CC@Co₉S₈-Co₄N cell shows the lightest colour and is within the smallest area, implying the most effective confinement of LiPSs in the S/CC@Co₉S₈-Co₄N heterostructures cathode over 100 cycles (Fig. S13†). These phenomena are well in accord with the electrochemical test results, and visually demonstrate that CC@Co₉S₈-Co₄N serves as a great sulfur host for LSBs. In Fig. S14,† it is shown that the fresh S/CC@Co₉S₈-Co₄N heterostructures cathode is able to power 30 red light-emitting diode (LED) flashlights. Owing to the outstanding conductivity and kinetics-favorable structure, the S/CC@Co₉S₈-Co₄N cathode reveals a quick rate response against various current rates. The discharge-charge curves of the S/CC@Co₉S₈-Co₄N electrodes exhibit a flattening feature with obvious plateau regions at different current rates (Fig. S15†). As a result, even when cycled at high current densities of 2.0 and 5.0C, high discharge capacities of 1049 and 648 mA h g⁻¹, respectively, could be maintained. These high capacities correspond to 77% and 47% of the discharge capacities at 0.2C. After deep cycling at 5.0C, a high capacity of 1136 mA h g⁻¹ (83.76% of the initial) could be recovered on abruptly switching back to 0.2C, suggesting the excellent electrochemical reversibility and electrode stability. In contrast, the S/CC@Co₉S₈, CC@Co₄N, and S/CC@PCNA cells exhibit much lower capacities at the corresponding currents. Most of the performance is irreversibly lost upon further increasing the current density (Fig. 5c). Such a high-rate capability is prominent over most carbon cloth-based cathodes (Fig. S16 and Table S2†). Since the high mass loading of active materials and high areal capacities are essential for the high energy density of LSBs, a S/CC@Co₉S₈-Co₄N electrode with areal sulfur loading of 1.4–2.0 mg cm⁻² was further evaluated (Fig. 5d). In addition, high energy density (342 W h kg⁻¹) and power density (700 W kg⁻¹) of S/CC@Co₉S₈-Co₄N were obtained (Table S3†). Upon cycling at 0.2C, an areal capacity of 3.3 mA h cm⁻² was delivered. When the current density was increased to 2.0 and 5.0C, the areal capacities were stabilized at above 2.1 mA h cm⁻² and 1.3 mA h cm⁻², respectively. The calculated potential differences between the discharge/charge voltage plateaus of S/CC@Co₉S₈ and S/CC@Co₉S₈-Co₄N at current rates of 0.2, 0.5, 1, 2, 3, 4, and 5.0C are shown in Fig. 5d. The polarization in the S/CC@Co₉S₈-Co₄N cathode is much alleviated compared to the S/CC@Co₉S₈ cathode at a wide range of current densities. These results further confirm that the S/CC@Co₉S₈-Co₄N heterostructures possess much less polarization and better reaction kinetics than S/CC@Co₉S₈. More importantly, on increasing the sulfur loading to 6.1 mg cm⁻² (Fig. 5e), the S/CC@Co₉S₈-Co₄N still delivers stable cycling performance with an outstanding performance discharge of 714 mA h g⁻¹ at 0.2C over 200 cycles.

The capacity decay is only 0.084% per cycle and a high retention of performance (83.0% of the initial) is achieved. Furthermore, the effects of sulfidation time on the heterostructures are shown in Fig. S17† and the resultant electrochemical properties of S/CC@Co₉S₈-Co₄N have been explored (Fig. 5f). The S/CC@Co₉S₈-Co₄N electrode from 1 h sulfidation shows an excellent cycling performance that outputs a discharge capacity of 776 mA h g⁻¹ over 500 cycles at 1.0C. However, the capacities of S/CC@Co₉S₈-Co₄N from 0.5, 2, and 4 h sulfidation under the same conditions decrease to 515, 374, and 126 mA h g⁻¹, respectively. Obviously, benefiting from the appropriate sulfidation time of 1 h, the S/CC@Co₉S₈-Co₄N electrode shows the highest cycling performance among these materials. Remarkably, the S/CC@Co₉S₈-Co₄N heterostructures electrode exhibits an ultra-long lifespan of 618 mA h g⁻¹ over 1000 cycles at 1.0C. Even when cycled at a high current density of 5.0C, the performance still possesses a stable capacity retention of over 70% in the whole cycling process, and nearly 100% coulombic efficiency after the activation process. This corresponds to an ultra-low capacity fading of 0.027% per cycle, suggesting the outstanding long-term stability for practical application. In contrast, the S/CC@Co₉S₈ electrode exhibits inferior cycling performance and fast capacity decay within 1000 cycles (Fig. 5g).

To get a deeper insight into the excellent electrochemical properties of the p-n heterostructures cathode discussed above, the surface interaction of the heterostructure composites and intermediate polysulfides during the whole discharge process at 0.5C was carefully evaluated *in situ* in a visual bottle lithium-sulfur cell. The bottle cells with S/CC@Co₉S₈ and S/CC cathodes were also prepared. As shown in Fig. 6a and S19,† at the 0.5 h interval, the electrolyte of the S/CC@Co₉S₈-Co₄N cell only exhibits the lightest yellow color compared with S/CC and S/CC@Co₉S₈. At the end of the reaction, it has only a negligible change, demonstrating the effective conversion to lithium sulfides. Hence, the bottle lithium sulfur cells confirm that the soluble polysulfide shuttle effect in the heterostructures cathode is effectively restrained.¹⁸

As shown in Fig. 6b, the CV curves of the symmetrical cells were recorded at 50 mV s⁻¹ within a voltage window of 0.8–0.8 V. The Li₂S₆-free cells show negligible contribution of current. With the addition of the Li₂S₆-containing electrolyte, both the Co₉S₈ and Co₉S₈-Co₄N symmetrical cells exhibit much higher current response. More importantly, the current response of the Co₉S₈-Co₄N symmetrical cell is much higher than that of the Co₉S₈ electrode, suggesting that the heterostructure nanoparticles significantly boost the kinetic lithiation/delithiation reaction in the polysulfide conversion.^{69–71} Considering that the symmetric cells are not affected by the lithium foil, the electrochemical impedance spectroscopy (EIS) of the symmetric cells was carried out to investigate the interfacial properties between the electrode and the polysulfides.⁷⁰ As shown in Fig. 6c, the heterostructures electrode shows much lower charge transfer resistance (R_{ct}) compared with S/CC@Co₉S₈, indicating the more rapid charge transfer attributed to the boosted kinetic redox reaction of polysulfide conversion induced by the heterostructure nanoparticles, which is in agreement with the CV results.

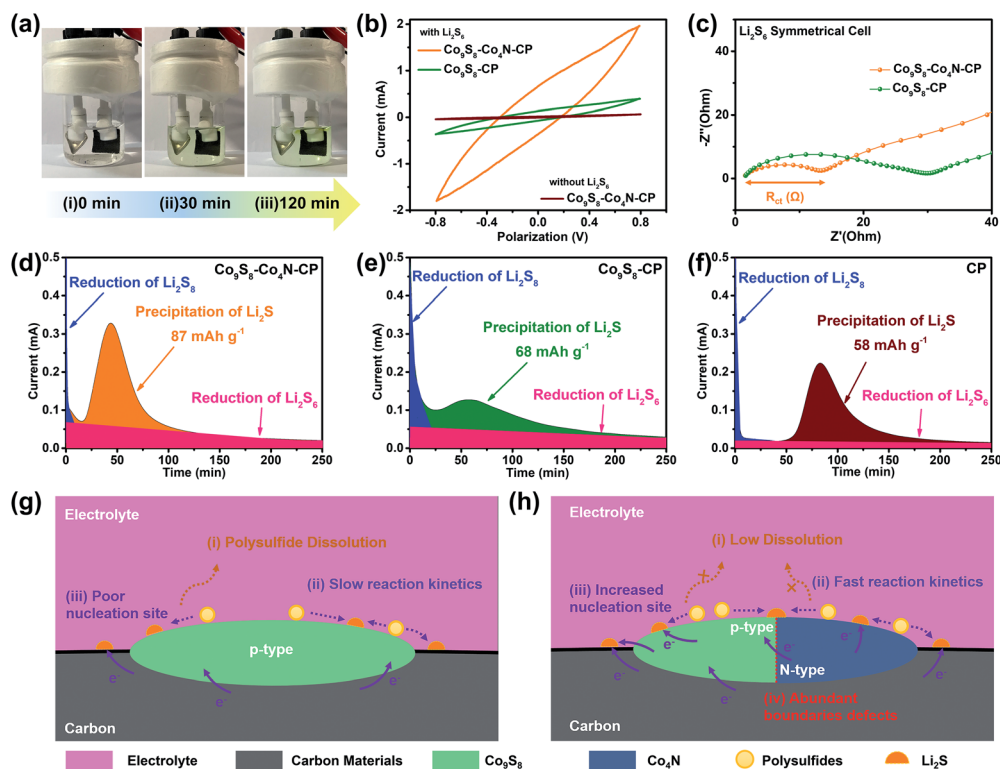


Fig. 6 (a) Digital photos of the bottle-cells indicating the excellent absorptivity of the S/CC@Co₉S₈–Co₄N composite. (b) Cyclic voltammograms of the symmetric cells of Co₉S₈–Co₄N-CP and Co₉S₈–CP electrodes with and without Li₂S₆ solution at a scan rate of 50 mV s⁻¹. (c) EIS of the symmetrical cells with Co₉S₈–Co₄N-CP and Co₉S₈–CP working electrodes. (d–f) Potentiostatic discharge curves at 2.05 V in Li₂S₆/tetraglyme solution on Co₉S₈–Co₄N-CP, Co₉S₈–CP, and CP, respectively. (g and h) Schematic illustration of the polysulfide adsorption/conversion processes on the CC@Co₉S₈ and CC@Co₉S₈–Co₄N heterostructure surfaces.

To further investigate the promotion of the liquid–solid conversion, potentiostatic Li₂S precipitation experiments were designed with fiber paper (CP), Co₉S₈-CP, and heterostructure-CP cathode based coin cells with Li₂S₆/tetraglyme catholyte.⁷² As shown in Fig. 6d–f, the responsivity of Li₂S nucleation for the heterostructures cathode was compared with pure CP or Co₉S₈-CP. Furthermore, even at a shorter nucleation time, the precipitation capacity of Li₂S on the Co₉S₈–Co₄N-CP heterostructure surface (87 mA h g⁻¹) is higher than those on pure CP (58 mA h g⁻¹) and Co₉S₈-CP (68 mA h g⁻¹). These results demonstrate that the heterostructure dramatically reduces the overpotential of Li₂S nucleation and enhances the precipitation of Li₂S.^{34,73}

It has been reported that Co₉S₈ has a strong adsorption for polysulfides,^{74–76} however, the conversion of the anchored LiPSs is difficult on the surface of Co₉S₈, as shown in Fig. 6g. As a result, sluggish electron transfer and incomplete electrochemical reactions are caused. In addition, Co₉S₈ provides limited number of active sites, therefore, the absorption of polysulfides at high sulfur loading is insufficient. Even worse, when the battery gets close to deep discharge, the anchoring/conversion is gradually interrupted due to the deposition of the insulating Li₂S on the carbon surface. Compared with the Co₉S₈, the Co₄N has drawn enormous attention as a result of its high conductivity (1.67 × 10⁵ S m⁻¹),⁴⁴ high catalytic activity,⁴⁸

and better inhibition of the shuttle effect.⁶⁷ Therefore, Fig. 6h shows that the composite containing the Co₉S₈–Co₄N heterostructures loaded onto the carbon cloth possesses the merits of both strong adsorption and catalytic conversion. The excellent electrochemical performance could be ascribed to the following reasons. Firstly, the strong polarity of Co₉S₈, Co₄N, and LiPSs effectively controls the outward diffusion of the polysulfides in the electrolytes, thus reducing the shuttle effect. Secondly, the abundant active sites and boundary defects constructed by the p–n heterostructures reduce the overpotential of Li₂S nucleation and improve the nucleation/conversion redox kinetics.⁷⁷ Thirdly, the heterostructures restrict the growth of the crystalline domains and could shorten the Li⁺ diffusion pathways.⁶²

4. Conclusions

In summary, we have designed a novel p–n heterostructure embedded within hollow carbon nanosheet arrays grown on carbon cloth by the combination of sulfidation and nitridation of the ZIF precursor. When used as the cathode host material for LSBs, this hollow structure can increase the sulfur loading, supply enough space for relieving the shuttle effect and the volume expansion of the whole cycling process. Moreover, the Co₉S₈–Co₄N heterostructures can reasonably limit the LiPSs' dissolution owing to the strong chemical adsorption and efficiently promote the conversion of the long-chain LiPSs/

Li₂S. Due to the structural and compositional superiorities, the free-standing S/CC@Co₉S₈-Co₄N cathode delivers a very slow capacity loss of 0.027% per cycle over 1000 cycles at 5.0C. Our work provides a new avenue for the construction of heterostructure materials towards energy storage and transformation.

Conflicts of interest

There are no conflicts to declare.

Acknowledgements

This work is supported by the National Natural Science Foundation of China (Grant No. 51672033, U1610105, U1610255).

Notes and references

- X. Ji, K. T. Lee and L. F. Nazar, *Nat. Mater.*, 2009, **8**, 500–506.
- Q. Pang, X. Liang, C. Y. Kwok, J. Kulisch and L. F. Nazar, *Adv. Energy Mater.*, 2017, **7**, 1601630.
- Z. Wang, Y. Dong, H. Li, Z. Zhao, H. B. Wu, C. Hao, S. Liu, J. Qiu and X. W. Lou, *Nat. Commun.*, 2014, **5**, 5002.
- R. Fang, S. Zhao, P. Hou, M. Cheng, S. Wang, H. M. Cheng, C. Liu and F. Li, *Adv. Mater.*, 2016, **28**, 3374–3382.
- L. Sun, D. Wang, Y. Luo, K. Wang, W. Kong, Y. Wu, L. Zhang, K. Jiang, Q. Li, Y. Zhang, J. Wang and S. Fan, *ACS Nano*, 2016, **10**, 1300–1308.
- K. Mi, Y. Jiang, J. K. Feng, Y. T. Qian and S. L. Xiong, *Adv. Funct. Mater.*, 2016, **26**, 1571–1579.
- H. H. Xu, L. Qie and A. Manthiram, *Nano Energy*, 2016, **26**, 224–232.
- Z. Li, J. Zhang and X. W. Lou, *Angew. Chem., Int. Ed.*, 2015, **54**, 12886–12890.
- S. L. Mei, C. J. Jafta, I. Laueremann, Q. Ran, M. Kargell, M. Ballauff and Y. Lu, *Adv. Funct. Mater.*, 2017, **27**, 1701176.
- H. Wei, E. F. Rodriguez, A. S. Best, A. F. Hollenkamp, D. Chen and R. A. Caruso, *Adv. Energy Mater.*, 2017, **7**, 1601616.
- Z. Li, J. Zhang, B. Guan, D. Wang, L. M. Liu and X. W. Lou, *Nat. Commun.*, 2016, **7**, 13065.
- X. Liang, C. Y. Kwok, F. Lodi-Marzano, Q. Pang, M. Cuisinier, H. Huang, C. J. Hart, D. Houtarde, K. Kaup, H. Sommer, T. Brezesinski, J. Janek and L. F. Nazar, *Adv. Energy Mater.*, 2016, **6**, 1501636.
- R. Elazari, G. Salitra, A. Garsuch, A. Panchenko and D. Aurbach, *Adv. Mater.*, 2011, **23**, 5641–5744.
- K. Xi, S. Cao, X. Peng, C. Ducati, R. V. Kumar and A. K. Cheetham, *Chem. Commun.*, 2013, **49**, 2192–2194.
- G. Li, J. Sun, W. Hou, S. Jiang, Y. Huang and J. Geng, *Nat. Commun.*, 2016, **7**, 10601.
- J. S. Lee, W. Kim, J. Jang and A. Manthiram, *Adv. Energy Mater.*, 2017, **7**, 1601943.
- J. Song, M. L. Gordin, T. Xu, S. Chen, Z. Yu, H. Sohn, J. Lu, Y. Ren, Y. Duan and D. Wang, *Angew. Chem., Int. Ed.*, 2015, **54**, 4325–4329.
- T. Lei, Y. Xie, X. Wang, S. Miao, J. Xiong and C. Yan, *Small*, 2017, **13**, 1701013.
- G. Babu, N. Masurkar, H. Al Salem and L. M. Arava, *J. Am. Chem. Soc.*, 2017, **139**, 171–178.
- Z. Yuan, H. J. Peng, T. Z. Hou, J. Q. Huang, C. M. Chen, D. W. Wang, X. B. Cheng, F. Wei and Q. Zhang, *Nano Lett.*, 2016, **16**, 519–527.
- F. Sun, J. Wang, D. Long, W. Qiao, L. Ling, C. Lv and R. Cai, *J. Mater. Chem. A*, 2013, **1**, 13283–13289.
- C. Zheng, S. Niu, W. Lv, G. Zhou, J. Li, S. Fan, Y. Deng, Z. Pan, B. Li, F. Kang and Q.-H. Yang, *Nano Energy*, 2017, **33**, 306–312.
- N. Mosavati, S. O. Salley and K. Y. S. Ng, *J. Power Sources*, 2017, **340**, 210–216.
- T.-G. Jeong, D. S. Choi, H. Song, J. Choi, S.-A. Park, S. H. Oh, H. Kim, Y. Jung and Y.-T. Kim, *ACS Energy Lett.*, 2017, **2**, 327–333.
- L. Li, L. Chen, S. Mukherjee, J. Gao, H. Sun, Z. Liu, X. Ma, T. Gupta, C. V. Singh, W. Ren, H. M. Cheng and N. Koratkar, *Adv. Mater.*, 2017, **29**, 1602734.
- J. Liang, L. Yin, X. Tang, H. Yang, W. Yan, L. Song, H. M. Cheng and F. Li, *ACS Appl. Mater. Interfaces*, 2016, **8**, 25193–25201.
- Y. Yang, K. Zhang, H. Lin, X. Li, H. C. Chan, L. Yang and Q. Gao, *ACS Catal.*, 2017, **7**, 2357–2366.
- C. Zhu, A. L. Wang, W. Xiao, D. Chao, X. Zhang, N. H. Tiep, S. Chen, J. Kang, X. Wang, J. Ding, J. Wang, H. Zhang and H. J. Fan, *Adv. Mater.*, 2018, **30**, 1705516.
- S. Deng, Y. Zhong, Y. Zeng, Y. Wang, X. Wang, X. Lu, X. Xia and J. Tu, *Adv. Sci.*, 2018, **5**, 1700772.
- W. Luo, F. Li, Q. Li, X. Wang, W. Yang, L. Zhou and L. Mai, *ACS Appl. Mater. Interfaces*, 2018, **10**, 7201–7207.
- T. Zhou, Y. Zhao, G. Zhou, W. Lv, P. Sun, F. Kang, B. Li and Q. H. Yang, *Nano Energy*, 2017, **39**, 291–296.
- L. Hu, C. Dai, H. Liu, Y. Li, B. Shen, Y. Chen, S.-J. Bao and M. Xu, *Adv. Energy Mater.*, 2018, **8**, 1800709.
- S. Shi, Z. Li, Y. Sun, B. Wang, Q. Liu, Y. Hou, S. Huang, J. Huang and Y. Zhao, *Nano Energy*, 2018, **48**, 510–517.
- T. Zhou, W. Lv, J. Li, G. Zhou, Y. Zhao, S. Fan, B. Liu, B. Li, F. Kang and Q.-H. Yang, *Energy Environ. Sci.*, 2017, **10**, 1694–1703.
- Y. Song, W. Zhao, L. Kong, L. Zhang, X. Zhu, Y. Shao, F. Ding, Q. Zhang, J. Sun and Z. Liu, *Energy Environ. Sci.*, 2018, **11**, 2620–2630.
- B. Long, M.-S. Balogun, L. Luo, W. Qiu, Y. Luo, S. Song and Y. Tong, *Adv. Energy Mater.*, 2018, **8**, 1701681.
- S. Tang, N. Lu, S. K. Ryu and H. S. Choi, *J. Phys. Chem. C*, 2007, **111**, 1820–1829.
- M. Lan, R.-M. Guo, Y. Dou, J. Zhou, A. Zhou and J.-R. Li, *Nano Energy*, 2017, **33**, 238–246.
- H. Hu, L. Han, M. Yu, Z. Wang and X. W. Lou, *Energy Environ. Sci.*, 2016, **9**, 107–111.
- T. Chen, L. Ma, B. Cheng, R. Chen, Y. Hu, G. Zhu, Y. Wang, J. Liang, Z. Tie, J. Liu and Z. Jin, *Nano Energy*, 2017, **38**, 239–248.
- H. Zhang, Z. Zhao, Y.-N. Hou, Y. Tang, Y. Dong, S. Wang, X. Hu, Z. Zhang, X. Wang and J. Qiu, *J. Mater. Chem. A*, 2018, **6**, 7133–7141.

- 42 Q. Sun, B. He, X. Q. Zhang and A. H. Lu, *ACS Nano*, 2015, **9**, 8504–8513.
- 43 H. Zhang, D. Tian, Z. Zhao, X. Liu, Y.-N. Hou, Y. Tang, J. Liang, Z. Zhang, X. Wang and J. Qiu, *Energy Storage Materials*, 2018, DOI: 10.1016/j.ensm.2018.12.005.
- 44 K. R. Yoon, K. Shin, J. Park, S. H. Cho, C. Kim, J. W. Jung, J. Y. Cheong, H. R. Byon, H. M. Lee and I. D. Kim, *ACS Nano*, 2018, **12**, 128–139.
- 45 L. B. Wang, W. B. Zhang, X. S. Zheng, Y. Z. Chen, W. L. Wu, J. X. Qiu, X. C. Zhao, X. Zhao, Y. Z. Dai and J. Zeng, *Nat. Energy*, 2017, **2**, 869–876.
- 46 H. Yan, Y. Xie, Y. Jiao, A. Wu, C. Tian, X. Zhang, L. Wang and H. Fu, *Adv. Mater.*, 2018, **30**, 1704156.
- 47 Y. Z. Li, T. T. Li, W. Chen and Y. Y. Song, *ACS Appl. Mater. Interfaces*, 2017, **9**, 29881–29888.
- 48 P. Chen, K. Xu, Z. Fang, Y. Tong, J. Wu, X. Lu, X. Peng, H. Ding, C. Wu and Y. Xie, *Angew. Chem., Int. Ed.*, 2015, **54**, 14710–14714.
- 49 N. Kornienko, J. Resasco, N. Becknell, C. M. Jiang, Y. S. Liu, K. Nie, X. Sun, J. Guo, S. R. Leone and P. Yang, *J. Am. Chem. Soc.*, 2015, **137**, 7448–7455.
- 50 C. Zhao, C. Yu, M. Zhang, Q. Sun, S. Li, N. Banis, X. Han, Q. Dong, J. Yang, G. Wang, X. Sun and J. Qiu, *Nano Energy*, 2017, **41**, 66–74.
- 51 G. Mohan Kumar, P. Ilanchezhian, A. Madhan Kumar, T. S. Shabi, S. Tamil Selvan, S. Suresh, S. U. Yuldashev and T. W. Kang, *CrystEngComm*, 2015, **17**, 5932–5939.
- 52 Y. Zhao, X. Huang, X. Tan, T. Yu, X. Li, L. Yang and S. Wang, *Appl. Surf. Sci.*, 2016, **365**, 209–217.
- 53 I. S. Amiin, X. Liu, Z. Pu, W. Li, Q. Li, J. Zhang, H. Tang, H. Zhang and S. Mu, *Adv. Funct. Mater.*, 2018, **28**, 1704638.
- 54 Y. Qiu, W. Li, W. Zhao, G. Li, Y. Hou, M. Liu, L. Zhou, F. Ye, H. Li, Z. Wei, S. Yang, W. Duan, Y. Ye, J. Guo and Y. Zhang, *Nano Lett.*, 2014, **14**, 4821–4827.
- 55 H. J. Peng, T. Z. Hou, Q. Zhang, J. Q. Huang, X. B. Cheng, M. Q. Guo, Z. Yuan, L. Y. He and F. Wei, *Adv. Mater. Interfaces*, 2014, **1**, 1400227.
- 56 Z. Guo, F. Wang, Z. Li, Y. Yu, A. G. Tamirat, H. Qi, J. Han, W. Li, L. Wang and S. Feng, *J. Mater. Chem. A*, 2018, **6**, 22096–22105.
- 57 L. L. Wu, Q. S. Wang, J. Li, Y. Long, Y. Liu, S. Y. Song and H. J. Zhang, *Small*, 2018, **14**, 1704035.
- 58 L. An, L. Huang, P. Zhou, J. Yin, H. Liu and P. Xi, *Adv. Funct. Mater.*, 2015, **25**, 6814–6822.
- 59 X. Tao, J. Wang, C. Liu, H. Wang, H. Yao, G. Zheng, Z. W. Seh, Q. Cai, W. Li, G. Zhou, C. Zu and Y. Cui, *Nat. Commun.*, 2016, **7**, 11203.
- 60 S. Rehman, T. Tang, Z. Ali, X. Huang and Y. Hou, *Small*, 2017, **13**, 1700087.
- 61 Z. M. Zheng, H. C. Guo, F. Pei, X. Zhang, X. Y. Chen, X. L. Fang, T. H. Wang and N. F. Zheng, *Adv. Funct. Mater.*, 2016, **26**, 8952–8959.
- 62 G. Fang, Z. Wu, J. Zhou, C. Zhu, X. Cao, T. Lin, Y. Chen, C. Wang, A. Pan and S. Liang, *Adv. Energy Mater.*, 2018, **8**, 1703155.
- 63 X. Zhu, W. Zhao, Y. Song, Q. Li, F. Ding, J. Sun, L. Zhang and Z. Liu, *Adv. Energy Mater.*, 2018, **19**, 1800201.
- 64 H. Wang, T. Zhou, D. Li, H. Gao, G. Gao, A. Du, H. Liu and Z. Guo, *ACS Appl. Mater. Interfaces*, 2017, **9**, 4320–4325.
- 65 J. Xu, W. Zhang, Y. Chen, H. Fan, D. Su and G. Wang, *J. Mater. Chem. A*, 2018, **6**, 2797–2807.
- 66 G. Zhou, J. Sun, Y. Jin, W. Chen, C. Zu, R. Zhang, Y. Qiu, J. Zhao, D. Zhuo, Y. Liu, X. Tao, W. Liu, K. Yan, H. R. Lee and Y. Cui, *Adv. Mater.*, 2017, **29**, 1603366.
- 67 D. R. Deng, F. Xue, Y. J. Jia, J. C. Ye, C. D. Bai, M. S. Zheng and Q. F. Dong, *ACS Nano*, 2017, **11**, 6031–6039.
- 68 C. Li, Z. Xi, S. Dong, X. Ge, Z. Li, C. Wang and L. Yin, *Energy Storage Materials*, 2018, **12**, 341–351.
- 69 H. J. Peng, Z. W. Zhang, J. Q. Huang, G. Zhang, J. Xie, W. T. Xu, J. L. Shi, X. Chen, X. B. Cheng and Q. Zhang, *Adv. Mater.*, 2016, **28**, 9551–9558.
- 70 R. Fang, S. Zhao, Z. Sun, D.-W. Wang, R. Amal, S. Wang, H.-M. Cheng and F. Li, *Energy Storage Materials*, 2018, **10**, 56–61.
- 71 H. Lin, L. Yang, X. Jiang, G. Li, T. Zhang, Q. Yao, G. W. Zheng and J. Y. Lee, *Energy Environ. Sci.*, 2017, **10**, 1476–1486.
- 72 F. Y. Fan, W. C. Carter and Y. M. Chiang, *Adv. Mater. Interfaces*, 2015, **27**, 5203–5209.
- 73 S. Huang, Y. V. Lim, X. Zhang, Y. Wang, Y. Zheng, D. Kong, M. Ding, S. A. Yang and H. Y. Yang, *Nano Energy*, 2018, **51**, 340–348.
- 74 Q. Pang, D. Kundu and L. F. Nazar, *Mater. Horiz.*, 2016, **3**, 130–136.
- 75 J. He, Y. Chen and A. Manthiram, *Energy Environ. Sci.*, 2018, **11**, 2560–2568.
- 76 C. Dai, J.-M. Lim, M. Wang, L. Hu, Y. Chen, Z. Chen, H. Chen, S.-J. Bao, B. Shen, Y. Li, G. Henkelman and M. Xu, *Adv. Funct. Mater.*, 2018, **28**, 1704443.
- 77 H. Yuan, H.-J. Peng, B.-Q. Li, J. Xie, L. Kong, M. Zhao, X. Chen, J.-Q. Huang and Q. Zhang, *Adv. Energy Mater.*, 2019, **9**, 1802768.